Subsurface Defect Detection in GPR Data Integrating Temporal and Spatial Features

Kehui Liu , Nan Deng , Yanxia Wang , Xuejun Tian , and Jian Cheng

Abstract—Ground penetrating radar (GPR) has emerged as a pivotal tool for subsurface explorations, particularly in detecting subsurface defects that might endanger structural integrity. While GPR B-scan data visually depict underground conditions, it represents the time delay and amplitude of the returned electromagnetic (EM) waves, making them complex to interpret due to both their image-like appearance and their inherent waveform changes. To address this complexity, this article introduces the novel temporal–spatial synthesis network, designed to harness both temporal and spatial features for enhanced subsurface defect detection in GPR B-scan data. The echo state network, underpinned by reservoir computing, is utilized to fit the GPR data and capture its "temporal features," emphasizing the temporal variations present in the EM waves. Concurrently, the convolutional neural network focuses on discerning "spatial features" from the B-scan images, spotlighting spatial patterns that possibly indicate subsurface defects. After extracting these temporal and spatial features, they are synthesized to form a comprehensive representation of the GPR data. The enhanced synthesized feature facilitates precise classification, resulting in heightened differentiation between normal and defect-contained subsurface areas. Experiments on real-world GPR datasets are conducted, with the results underscoring the efficacy of the proposed approach.

Index Terms—B-scan data, convolutional neural network (CNN), echo state network (ESN), ground penetrating radar (GPR).

I. INTRODUCTION

GROUND penetrating radar (GPR) stands as a prominent noninvasive geophysical tool that employs electromagnetic (EM) waves to investigate and delineate subsurface structures and anomalies. By transmitting short pulses of EM waves into the ground, GPR offers a window into the subsurface, making it a crucial instrument for a myriad of geophysical and archaeological investigations [1]. As these EM waves propagate beneath the surface, they undergo interactions with various subsurface materials and boundaries, and their behavior provides a wealth of information about the underlying structure and composition [2]. Changes in material properties, such as transitions from soil to a buried artifact, a pipe, or a void, lead to distinct reflections. These reflections cause a portion of the wave energy to bounce back to the surface, which is then recorded and analyzed to decipher the subsurface environment and potential objects.

GPR B-scan data, while rich in detail, requires nuanced analysis, especially when targeting specific objectives, such as underground pipeline mapping [3] and the identification of subsurface hazards [4]. Pipelines introduce a distinct contrast in the subsurface EM properties. When analyzing GPR B-scan data for pipeline detection, one looks for hyperbolic reflections indicative of cylindrical objects [5]. The apex of these hyperbolas typically denotes the pipeline's position [6]. The pipeline depth and size can be estimated by fitting the hyperbola.

GPR B-scan data are equally pivotal when scouting for potential underground disasters, such as voids, sinkholes, or unstable zones that could lead to land subsidence. In this context, the B-scan data might exhibit irregular or absent reflections, indicating areas where the EM waves are not being reflected back due to a void or are being diffusely scattered by unstable zones. Accurate interpretation in this scenario could be challenging, as misidentifications have significant safety implications.

For the analysis of GPR data aimed at subsurface defects, several methodologies have been advanced. These include approaches rooted in permittivity [7], [8] and techniques centered on EM-wave manipulation [9], [10], [11]. In the realm of machine learning (ML), tools such as the support vector machine (SVM) [12] and support vector regression [13] have found application in GPR subsurface discernment. Furthermore, image characterization through Haar [14] and histograms of oriented gradient (HOG) [15] has been coupled with ML algorithms to sharpen the granularity of GPR data classification.

In recent times, deep learning (DL) techniques, predominantly centered on convolutional neural networks (CNNs), have garnered attention for object and anomaly detection in GPR and other remote sensing datasets [16], [17], [18], [19], [20], [21]. Amplifying this progression, Liu et al. [22] presented the "GPRInvNet," a model tailored to transform GPR B-Scan data into permittivity maps, skillfully pinpointing tunnel lining flaws. Similarly, Hou et al. [23] employed the mask scoring R-CNN, enhancing it with a unique anchoringsystem specifically for GPR data. They utilized transfer learning to accommodate varied GPR datasets. Further adding to this, Liu et al. [24]
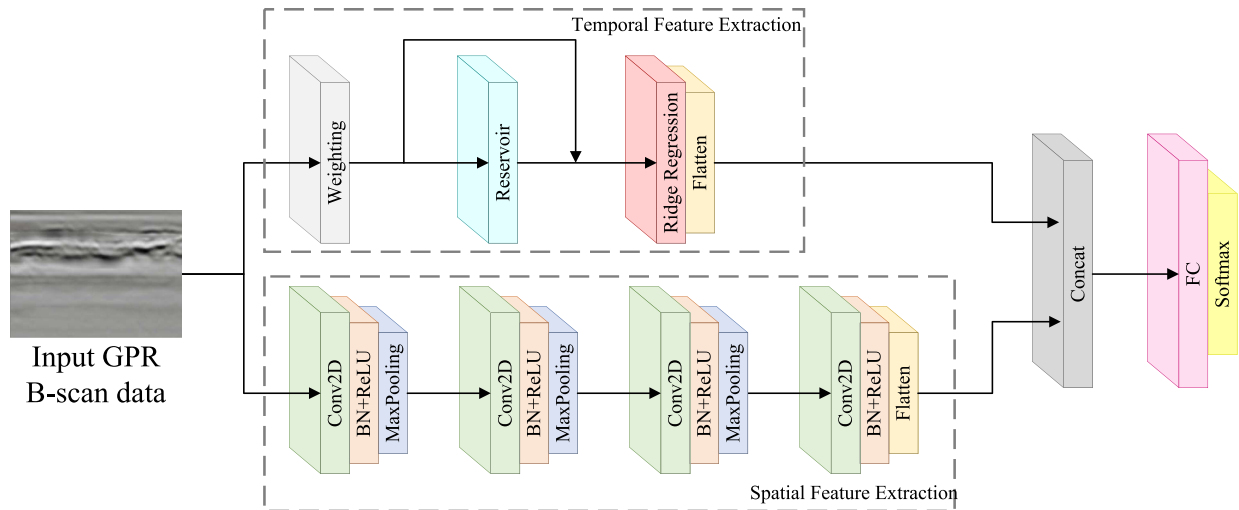
Fig. 1. TSSNet combines ESN's temporal feature extraction with CNN's spatial feature extraction for subsurface defect detection. ESN, based on reservoir computing, captures temporal features of GPR data by fitting the changing patterns in the data sequence, while CNN identifies spatial patterns in GPR B-scan data through convolutional and pooling layers. These features are then merged and processed for comprehensive subsurface defect detection.

refined YOLOv3 by incorporatingfour-scale detection layers, enhancing its capability to detect pavement cracks through GPR. The CNN-based approach interprets B-scan data from a visual perspective, treating them as image formats. Leveraging the synergy of convolution and pooling etc. operations, this approach extracts rich visual "spatial features," facilitating the distinction between patterns formed by various types of subsurface objects. Nonetheless, it is imperative to recognize that GPR data fundamentally encapsulates EM waves. The changing characteristics of these waveforms, termed "temporal features," are indicative of changes in the underground medium. Such dynamism is critical and should be judiciously considered in the detection of underground defects.

For subsurface defect detection, this article proposes the temporal–spatial synthesis network (TSSNet) that integrates the "temporal feature" extraction prowess of the echo state network (ESN) with the intricate "spatial feature" extraction of CNN. The TSSNet is illustrated in Fig. 1. The ESN is employed to capture and describe the temporal features within the GPR data, which is structured based on reservoir computing. The reservoir, inherent to the ESN, operates as a recurrent neural network with sparsely connected neurons. Its primary role is to integrate sequential data to compute the hidden states. Following this, by fitting the hidden states to the input data through a "next item prediction task," the ridge regression is utilized to accurately discern the associations between neighboring items, facilitating the extraction of intrinsic changing patterns within the data. Apart from the above-mentioned, the CNN module is dedicated to extracting spatial features. It comprises a series of convolutional layers, accompanied by batch normalization (BN) and pooling layers, designed to identify distinct patterns and hierarchies within the GPR B-scan data. As the data progresses through this cascade of layers, it undergoes transformations highlighting increasingly refined spatial representations. Upon extracting both temporal and spatial features from the GPR data, TSSNet flattens these features into 1-D vectors, which are

then concatenated to form a comprehensive feature vector. This concatenated vector is subsequently processed through a fully connected layer, which synthesizes the combined insights and performs the final classification task, thus enabling the holistic detection of subsurface defects within the GPR data.

Through experimentation on real-world GPR data, we observed that TSSNet, by integrating both temporal and spatial features, consistently exhibits considerable classification performance for detecting underground defects in GPR data. Moreover, when juxtaposed against conventional CNN-based DL models, TSSNet demonstrates enhanced stability, especially in scenarios with limited training data. This heightened stability can be attributed to the ESN's adeptness at capturing and extracting temporal features, complemented by the streamlined architecture of the CNN component within TSSNet.

The rest of this article is organized as follows. Section II details the TSSNet, extracting temporal and spatial features from GPR data. Experimental results are discussed in Section III. Finally, Section IV concludes this article.

II. METHODOLOGY

The proposed TSSNet consists of two primary modules: the ESN for temporal feature extraction and the CNN for spatial feature extraction from GPR data. In this section, we provide an in-depth exploration of each module, followed by the training and subsurface defect detection process.

A. Temporal Feature Extraction Through ESN

The ESN is a specialized form of a recurrent neural network characterized by a randomly generated reservoir and a learnable output layer. The architecture, in particular, the reservoir, plays a pivotal role in the handling of temporal dynamics. This reservoir comprises a large number of sparsely interconnected neurons, allowing for diverse signal pathways and the potential for intricate signal transformations. These properties ensure that
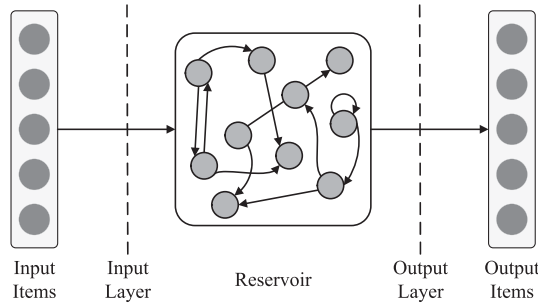
Fig. 2. General architecture of an ESN. It consists of an input layer, a reservoir, and an output layer. The input layer channels input into the reservoir, which captures temporal variations. The reservoir state is then mapped to the output layer to generate the final output items.

the reservoir has a vast memory capacity, capable of retaining historical input information over varying time scales.

In TSSNet, the primary objective of ESN is to extract temporal features from the GPR data, emphasizing the associations between neighboring input items. Existing works [25], [26], [27], [28] have demonstrated that by fitting sequential data with ESNs, the output weights effectively capture the variation patterns among adjacent items, serving as the extracted "temporal features" for subsequent analysis or classification.

As presented in Fig. 2, the ESN architecture consists of three primary layers: the input layer, which weights the input data and maps it to the reservoir; the reservoir itself, a dense collection of recurrently connected neurons; and the output layer, which linearly combines hidden states to produce the desired output.

Given a GPR B-scan block with K pixels in the vertical (depth) direction and T pixels in the horizontal (detection) direction, where the gray value at position (k, t) is $u_{k,t}$, we interpret each column's gray values as a whole item: $\mathbf{u}(t) = (u_{1,t}, u_{2,t}, \ldots, u_{K,t})^T$. This transforms the original data into a sequence of input items along the horizontal direction. Then, the hidden state of each item $\mathbf{x}(t)$ update as follows:

$$\mathbf{x}(t) = \tanh(\mathbf{W}\mathbf{x}(t-1) + \mathbf{W}_{\text{in}}\mathbf{u}(t)) \qquad (1)$$

where $\mathbf{W}_{\text{in}}$ is the input weight matrix, and $\mathbf{W}$ is the reservoir weight matrix. The output $\mathbf{y}(t)$ is subsequently computed as follows:

$$\mathbf{y}(t) = \mathbf{W}_{\text{out}}\mathbf{x}(t) + \mathbf{b} \qquad (2)$$

where $\mathbf{W}_{\text{out}}$ is the output weight matrix, and $\mathbf{b}$ is a bias vector.

Given that hidden states encapsulate the sequential information within the data, we implement a "next item prediction task" [25], which maps the hidden state $\mathbf{h}(t)$ to approximate the subsequent input item $\mathbf{u}(t+1)$. In other words, we aim to make the output $\mathbf{y}(t)$ approximate the next input item $\mathbf{u}(t+1)$. This procedure refers to determining the optimal output weights $\mathbf{W}_{\text{out}}$, which can be solved by collecting the hidden states and employing ridge regression to compute

$$\mathbf{W}_{\text{out}} = (\mathbf{X}^T\mathbf{X} + \lambda\mathbf{I})^{-1}\mathbf{X}^T\mathbf{Y} \qquad (3)$$

TABLE I
SPECIFICATIONS OF THE CNN ARCHITECTURE USED FOR SPATIAL FEATURE EXTRACTION

Layer type	Channels	Kernel size	Padding	Stride
Conv1	32	3×3	1	2
MaxPooling	–	2×2	0	1
Conv2	64	5×5	2	1
MaxPooling	–	2×2	0	3
Conv3	64	5×5	2	1
MaxPooling	–	2×2	0	2
Conv4	32	3×3	1	1

where $\mathbf{X}$ denotes the matrix of hidden states, $\mathbf{Y}$ represents the matrix of desired outputs (i.e., the next input items), λ is the regularization coefficient, and $\mathbf{I}$ stands for the identity matrix.

Owing to the unique role of the output layer that associates the current hidden state with future inputs, it becomes evident that it inherently captures the variation patterns between adjacent input items [29]. Consequently, we regard the solved output weights $\mathbf{W}_{\text{out}}$ as the temporal features of the original input data. These features serve as crucial information for subsequent classification and subsurface defect detection.

B. Spatial Feature Extraction With CNN

Given that the utilization of ESN and the "next item prediction task" primarily focuses on the temporal variation within the data, we also introduce a module based on CNN to extract spatial features from the GPR data.

As shown in Fig. 1, the CNN module commences with a 2-D convolutional layer (Conv2D), followed by BN and ReLU activation. A max-pooling layer then reduces the spatial dimensions while preserving essential features. The convolutional layer contains multiple filters to extract spatial hierarchies and patterns from the input data, while the BN layers stabilize the internal activation, ensuring a more consistent and effective learning process. The pooling layers play a crucial role in down-sampling the spatial dimensions, which not only reduces the computation but also enables the extraction of higher level abstract features. This structure is reiterated in the next two blocks, each consisting of Conv2D, BN, and ReLU layers. The final block, however, eschews pooling in favor of a flatten operation, converting the multidimensional feature maps into a 1-D vector.

This CNN module effectively captures the spatial information present in the GPR data by extracting and hierarchically organizing visual patterns, such as edges, textures, and other structural details. This hierarchical extraction and the resulting flattened vector provide a comprehensive representation of the spatial characteristics of the GPR data. Consequently, the output vector of this CNN module is regarded as the spatial feature and serves as crucial indicator for defect detection when combined with the temporal feature derived from the ESN module. For a granular breakdown of our CNN architecture, Table I encapsulates the specifics of each layer.
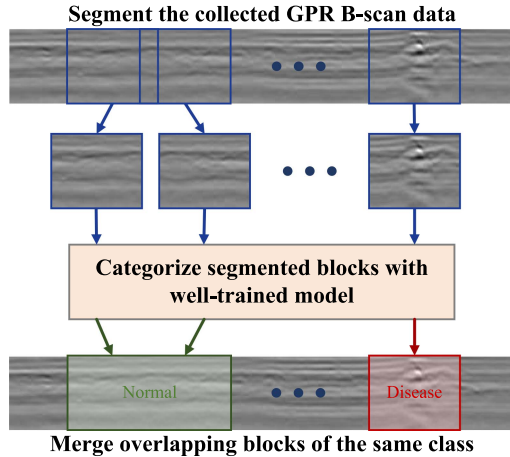
Fig. 3.　Workflow for subsurface defect detection. Collected GPR B-scan data are segmented into blocks, categorized by the well-trained TSSNet. Adjacent or overlapping blocks of the same class are then merged for a continuous representation of defect regions.

C. Training and Subsurface Defect Detection

The procedure of subsurface defect detection in our method can be divided into the training stage and defect detection. Initially, the available labeled GPR data are segmented into equal-sized blocks, with potential overlaps. Each block possesses a label, indicating the type of data it contains (normal or a kind of subsurface defect). With this collection of labeled blocks, our proposed model is primed for training. The optimization of the model parameters is accomplished through gradient descent, guided by the cross-entropy loss function, mathematically represented as

$$L(Y, \hat{Y}) = -\frac{1}{N} \sum_{i=1}^{N} \sum_{j=1}^{C} y_{ij} \log(\hat{y}_{ij}) \qquad (4)$$

where N is the total number of labeled blocks, C is the total number of classes, y_{ij} is a variable that is 1 if the ith block belongs to class j and 0 otherwise, $\hat{y}_{ij}$ denotes the predicted probability of the ith block being classified as class j.

The process of detection stage is depicted in Fig. 3. The subsequently collected data are first segmented and resized into blocks of the same size as in training. These blocks are then classified using the well-trained model to pinpoint any subsurface defects. To detect defects that span multiple blocks, adjacent or overlapping blocks with consistent data types are merged. This strategic amalgamation allows for a more coherent representation of the subsurface defect, enabling more accurate and comprehensive defect detection within the GPR data.

III. EXPERIMENTAL STUDY

This section presents the experimental studies of detecting subsurface defects using real-world GPR B-scan data. The utilized real-world data are first introduced. Comparative works are then presented, along with the specific analysis of experimental results.

	Type	Number
Normal	Concrete road	500
	Unpaved road	500
Defect	Cavity	312
	Crack	351
	Looseness	327
	Water-rich	305

A. Experimental Data and Settings

The GPR B-scan data we used are sourced from concrete and unpaved roads, prevalent in urban cities. Around 2300 GPR blocks were chosen.[1] Table II outlines the count and ratio of normal and different defect GPR data. In our tests, "normal" data indicates GPR readings from roads without underground issues (such as cavities) or structures (e.g., pipelines). "Defect" data denotes GPR readings capturing underground irregularities. The surveyed roads are frequently used urban roads. While multiple underground irregularities exist beneath them, sections with subsurface issues or structures are few.

In our experiments, major subsurface defects appear, including cavities, looseness, horizontal cracks, and water-rich.

1) "Cavity" beneath roads represents an underground space primarily air-filled, with often inconsistent contours. It contributes to road subsidence in cities. The dielectric difference between air and nearby substances leads to pronounced EM wave reflections upon cavity contact. Multiple internal reflections, and occasionally diffractions, may ensue.
2) "Looseness" pertains to soil that exhibits increased porosity and reduced density compared to neighboring soil with analogous moisture content. It diminishes the binding of soil grains, risking potential cave-ins and void development. This state resembles a blend of soil and air, with its varied soil attributes prompting erratic GPR reflections.
3) "Crack" hints at horizontal voids in the underground structure, predominantly filled with air. As waves intersect these voids, they generate waveform inconsistencies. During these detections, simultaneous waveform shifts could be observed.
4) "Water-rich" refer to regions where the concentration of water is higher than in surrounding areas, primarily consisting of water. These regions exhibit a higher dielectric constant than the nearby soil. Consequently, when EM waves interact with these regions, the amplitude of the reflected wave is typically more pronounced, while the energy of the EM wave decreases rapidly.

---

[1]Each block measures 150×150 pixels. The vertical extent of the original GPR B-scan data is 310 pixels, equating to a 60 ns time window (or a two-way travel time range) and an estimated depth of approximately 5–6 m underground. Given the underground defects for this test are between 0.5–2 m deep, we chose a vertical span of 50–200 pixels (roughly 10–40 ns) and a horizontal span of 150 pixels (around 3 m horizontally).
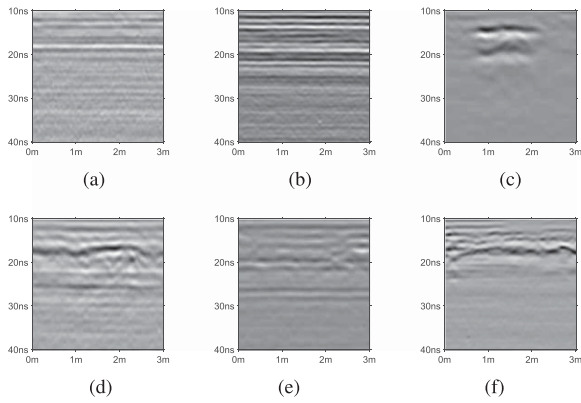
Fig. 4. These subfigures show several examples of segmented GPR B-scan data blocks in the conducted experiment. The subfigures (a) and (b) refer to normal data from concrete and unpaved roads, respectively. (a) Normal. (b) Normal. (c) Cavity. (d) Crack. (e) Looseness. (f) Water-rich.

Fig. 4 shows some examples of segmented GPR data blocks. The workflow for building the utilized dataset is as follows.

- *Collection and annotation of GPR data*
1) The process begins with the systematic collection of GPR data across the designated detection area, covering various subsurface conditions.
2) Postcollection, the data are meticulously reviewed for identifying and labeling different types of subsurface anomalies, such as cavities, cracks, and water-rich zones.
3) Expert interpretation is essential in this phase to ensure the accuracy of annotations, forming the foundation for subsequent model training and validation.
- *Data extraction and categorization*
1) For regions without anomalies ("normal"), data blocks are extracted randomly to represent a diverse range of subsurface conditions.
2) In contrast, for areas with identified anomalies, blocks are extracted using a fixed step size, covering the entire anomaly to ensure comprehensive representation.
3) Each block from anomalous regions is categorized based on the type of defect it contains, grouping similar anomaly blocks together.
4) This meticulous process ensures the dataset captures both the diversity within and distinctions between different types of subsurface defects.

Manipulations are performed on GPR B-scan data to suppress noise and emphasize subsurface features. This involves three primary steps: negating unwanted surface echoes, reducing noise, and offsetting propagation losses. Initially, the reflectance from the ground surface is eliminated. Then, a conventional median filter is applied to the data, reducing EM noise and interference [30]. Subsequently, the signal is adjusted with a time-dependent gain to compensate for losses due to medium attenuation and the radial dispersion of signal energy [31]. Our approach to gain manipulation is bifurcated into two main phases as follows.

- Initially, we identify and exclude sections with excessively high wave intensity. After this exclusion, we apply gain manipulation to the filtered data.

- In the second phase, we utilize a time-varying gain technique, wherein the gain exponent increases with the depth of detection. This helps in amplifying signal variations without inducing oversaturation. If oversaturation is observed in data collected from roads, we modify the gain settings for all data from that specific road, ensuring the retention of variable information. This fine-tuning process is manually executed.

For the implementation of the ESN layer in TSSNet, we employed a grid search method to determine the optimal hyperparameters. The reservoir size was chosen from a set of {50, 100, 200}, and the spectral radius ranged from 0.2 to 1, in increments of 0.2. Input scaling was selected from {0.5, 1, 2}. In addition, input weights and reservoir weights were randomly initialized following a standard normal distribution. The sparsity of the reservoir connections was set to a default value of 0.1, and the regularization coefficient for ridge regression was fixe at 1. These settings were carefully chosen to balance the model's complexity with its performance on our GPR B-scan dataset. In addition, the experiment is repeated five times with different random seeds, and the average results are reported.

B. Experiments and Comparisons

Experiments under different proportions of training and test data are conducted. The proposed method is compared with two types of methods as follows.

- Traditional image feature extraction methods including HOG [15] and Haar [14] that could extract features from the data directly, followed by SVM for classification.
- DL methods including ResNet18 [32], ResNet50 [33], VGG16 [34], and VGG19 [34] that could directly classify the segmented GPR B-scan data block into classes.

The obtained results are presented in Table III, and Fig. 5 further illustrates the confusion matrices of the classification results by TSSNet at different training proportions. We also present examples of recognition results for each type of defect in Fig. 6. Traditional image feature extraction methods, such as Haar and HOG, rely on predefined kernels or patterns to identify specific features in an image. For instance, Haar-like features emphasize abrupt intensity changes in localized regions, while HOG captures gradient distributions. Although these methods have proven effective in many applications, they are inherently static and predefined, limiting their adaptability and performance in discerning the nuances of GPR data.

DL methods, particularly those based on CNN architectures, introduce a paradigm shift. Unlike traditional methods, CNNs learn to identify patterns and features directly from the data, eliminating the need for handcrafted kernels. Techniques such as VGG and ResNet employ deep architectures with multiple layers, each responsible for extracting increasingly abstract and intricate features. The depth and flexibility of these architectures allow them to capture complex patterns, especially when there are sufficient data to learn from. The process of gradient descent continually refines the feature extraction capabilities, but this iterative optimization process in complex and deep networks

TABLE III
COMPARATIVE ANALYSIS OF DETECTION METHODS USING GPR DATA

Training proportion	90%			70%			50%		
	Pre	Rec	F1	Pre	Rec	F1	Pre	Rec	F1
Haar+SVM	87.09%	86.78%	86.93%	81.91%	82.3%	82.1%	81.48%	79.96%	80.71%
HOG+SVM	86.56%	83.76%	85.14%	85.34%	82.76%	84.03%	83.01%	81.31%	82.15%
VGG-16	94.28%	94.38%	94.33%	93.32%	92.16%	92.74%	89.02%	89.37%	89.19%
VGG-19	95.26%	94.56%	94.91%	93.89%	91.06%	92.45%	88.94%	87.97%	88.45%
ResNet-18	95.26%	94.65%	94.95%	93.66%	93.87%	93.76%	90.12%	92.15%	91.12%
ResNet-50	96.75%	96.28%	96.51%	93.05%	93.7%	93.37%	90.44%	90.97%	90.7%
Proposed TSSNet	97.08%	97.14%	97.11%	96.91%	96.34%	96.62%	94.55%	93.88%	94.21%

This table presents a performance comparison of the proposed TSSNet against established baselines (Haar+SVM, HOG+SVM, VGG-16, VGG-19, ResNet-18, ResNet-50) across different training proportions (90%, 70%, and 50%) based on precision (Pre), recall (Rec), and F1-score (F1) metrics.
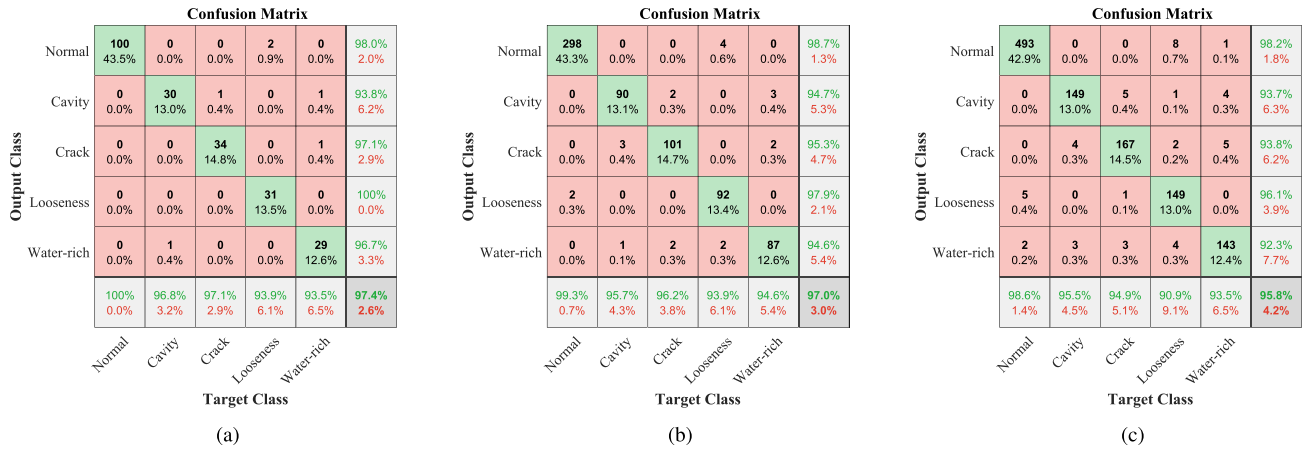

Fig. 5. Subfigures display the confusion matrices of the classification results by TSSNet at training proportions of 90%, 70%, and 50%, respectively. (a) 90% training. (b) 70% training. (c) 50% training.
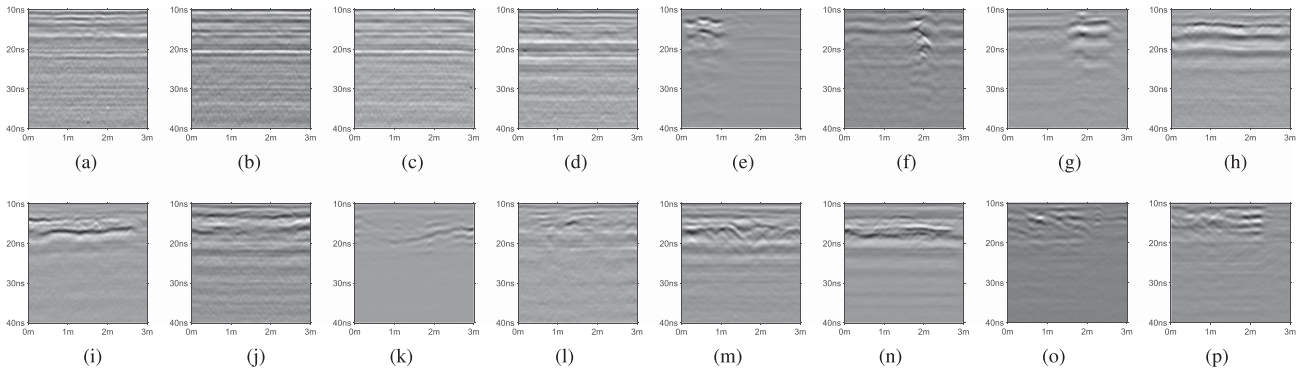

Fig. 6. Examples of recognition results for each type of defect. (a) Normal. (b) Normal. (c) Normal. (d) Normal. (e) Cavity. (f) Cavity. (g) Cavity. (h) Crack. (i) Crack. (j) Crack. (k) Looseness. (l) Looseness. (m) Looseness. (n) Water-rich. (o) Water-rich. (p) Water-rich.

necessitates a large training dataset to avoid overfitting and to ensure generalization.

GPR data presents unique characteristics compared with visual images. As a visual representation of EM waves reflecting off subsurface objects or structures, it captures more than just spatial variations. Temporal variations-how wave reflections change over time or position-offer critical insights. Traditional image processing or even standard CNNs might overlook these temporal variations.

The proposed TSSNet not only capitalizes on the robust feature extraction capabilities of CNNs but also integrates the temporal variations inherent in GPR data. Evident from Fig. 7, by incorporating the ESN, TSSNet captures and learns from the time-based variations present in the GPR scans. ESN, with
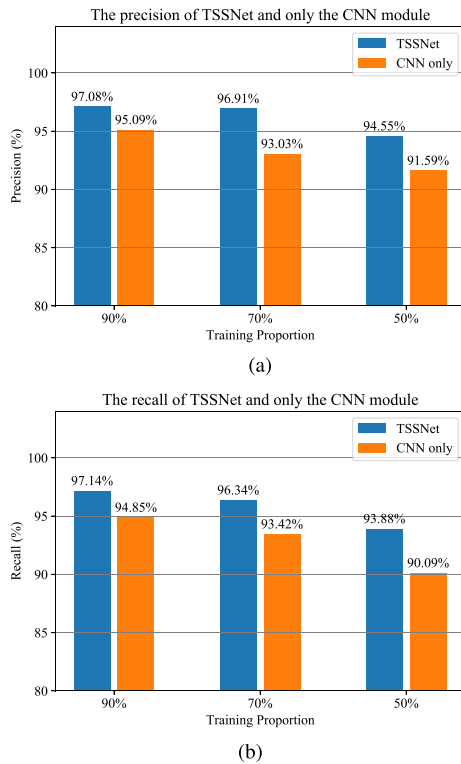
Fig. 7. These subfigures illustrate the precision and recall of TSSNet, comparing configurations with and without the ESN module. The results highlight the significance of temporal features in identifying underground defects. Note the "CNN only" refers to the CNN module of the TSSNet. (a) Precision. (b) Recall.

its reservoir computing mechanism, can recognize patterns in temporal sequences, making it especially potent in discerning the variation patterns of the GPR data. The fusion of spatial understanding from the CNN and temporal insights from the ESN in TSSNet provides a more holistic understanding of the GPR scans, leading to improved classification outcomes.

IV. CONCLUSION

GPR has provided invaluable insights into subsurface structures and anomalies, leveraging EM waves to uncover what lies beneath. The intricate patterns and behaviors exhibited in GPR B-scan data necessitate sophisticated analysis tools, especially when pinpointing specific subsurface objectives, from underground pipelines to potential hazards. This article presented the TSSNet, a novel approach that harmoniously marries the temporal feature extraction capabilities of ESN with the spatial prowess of CNN. Through rigorous structuring based on reservoir computing, the ESN module effectively captured the changing characteristics of the GPR data's waveforms. Simultaneously, the CNN module meticulously extracted spatial features, bringing out patterns and hierarchies within the data. The subsequent integration of these two facets led to a synthesized understanding that bolstered the detection of subsurface defects. Building on TSSNet, future work will focus on refining its architectures for more specialized scenarios, possibly incorporating additional sensors' data to create a multimodal

approach. Furthermore, the exploration of alternative few-short learning architectures and training strategies may yield even better performance.

REFERENCES

[1] D. Daniels, "Ground penetrating radar," *Inst. Eng. Technol.*, vol. 1, pp. 353–379, 2004.

[2] X. Zhou, H. Chen, and T. Hao, "Efficient detection of buried plastic pipes by combining GPR and electric field methods," *IEEE Trans. Geosci. Remote Sens.*, vol. 57, no. 6, pp. 3967–3979, Jun. 2019.

[3] X. Zhou, Q. Chen, B. Jiang, and H. Chen, "An underground pipeline mapping method based on fusion of multisource data," *IEEE Trans. Geosci. Remote Sens.*, vol. 60, 2022, Art. no. 4511711.

[4] X. Zhou et al., "Underground anomaly detection in GPR data by learning in the C3 model space," *IEEE Trans. Geosci. Remote Sens.*, vol. 61, 2023, Art. no. 5110511.

[5] G. Jiang, X. Zhou, J. Li, and H. Chen, "A cable-mapping algorithm based on ground-penetrating radar," *IEEE Geosci. Remote Sens. Lett.*, vol. 16, no. 10, pp. 1630–1634, Oct. 2019.

[6] X. Zhou, Q. Chen, S. Lyu, and H. Chen, "Mapping the buried cable by ground penetrating radar and Gaussian-process regression," *IEEE Trans. Geosci. Remote Sens.*, vol. 60, 2022, Art. no. 4509912.

[7] M. I. Hammons, H. Von Quintus, G. M. Geary, P. Y. Wu, and D. M. Jared, "Detection of stripping in hot-mix asphalt," *Transp. Res. Rec.*, vol. 1949, no. 1, pp. 20–31, 2006.

[8] C. Plati and A. Loizos, "Estimation of in-situ density and moisture content in HMA pavements based on GPR trace reflection amplitude using different frequencies," *J. Appl. Geophys.*, vol. 97, pp. 3–10, 2013.

[9] W. He, T. Hao, W. Zheng, and H. Ke, "Time-frequency analysis of a flexible RF sensor for GPR applications," in *Proc. Photon. Electromagnetics Res. Symp.-Fall*, 2019, pp. 610–616.

[10] M. A. Rasolet al., "GPR laboratory tests and numerical models to characterize cracks in cement concrete specimens, exemplifying damage in rigid pavement," *Measurement*, vol. 158, 2020, Art. no. 107662.

[11] T. Hao, L. Jing, and W. He, "An automated GPR signal denoising scheme based on mode decomposition and principal component analysis," *IEEE Geosci. Remote Sens. Lett.*, vol. 20, 2023, Art. no. 3500105.

[12] F. Ye, Z. Zhang, K. Chakrabarty, and X. Gu, "Board-level functional fault diagnosis using multikernel support vector machines and incremental learning," *IEEE Trans. Comput.-Aided Des. Integr. Circuits Syst.*, vol. 33, no. 2, pp. 279–290, Feb. 2014.

[13] A. J. Smola and B. Schölkopf, "A tutorial on support vector regression," *Statist. Comput.*, vol. 14, pp. 199–222, 2004.

[14] P. Klsk, A. Godziuk, M. Kapruziak, and B. Olech, "Fast analysis of C-scans from ground penetrating radar via 3-D haar-like features with application to landmine detection," *IEEE Trans. Geosci. Remote Sens.*, vol. 53, no. 7, pp. 3996–4009, Jul. 2015.

[15] N. Dalal and B. Triggs, "Histograms of oriented gradients for human detection," in *Proc. IEEE Comput. Soc. Conf. Comput. Vis. Pattern Recognit.*, 2005, pp. 886–893.

[16] U. Ozkaya, F. Melgani, M. B. Bejiga, L. Seyfi, and M. Donelli, "GPR B scan image analysis with deep learning methods," *Measurement*, vol. 165, 2020, Art. no. 107770.

[17] B. Huang, Y. Zhu, M. Usman, X. Zhou, and H. Chen, "Graph neural networks for missing value classification in a task-driven metric space," *IEEE Trans. Knowl. Data Eng.*, vol. 35, no. 8, pp. 8073–8084, Aug. 2023.

[18] Z. Tong, D. Yuan, J. Gao, and Z. Wang, "Pavement defect detection with fully convolutional network and an uncertainty framework," *Comput.-Aided Civil Infrastructure Eng.*, vol. 35, no. 8, pp. 832–849, 2020.

[19] Y. Zhu, B. Huang, X. Zhou, and H. Chen, "Level-wise dynamic label assignment for oriented object detection," in *Proc. IEEE Symp. Ser. Comput. Intell.*, 2022, pp. 1304–1311.

[20] C. Ren, X. Wang, J. Gao, X. Zhou, and H. Chen, "Unsupervised change detection in satellite images with generative adversarial network," *IEEE Trans. Geosci. Remote Sens.*, vol. 59, no. 12, pp. 10047–10061, Dec. 2021.

[21] X. Wang et al., "Accurate label refinement from multiannotator of remote sensing data," *IEEE Trans. Geosci. Remote Sens.*, vol. 61, 2023, Art. no. 4700413.

[22] B. Liu et al., "GPRInvNet: Deep learning-based ground-penetrating radar data inversion for tunnel linings," *IEEE Trans. Geosci. Remote Sens.*, vol. 59, no. 10, pp. 8305–8325, Oct. 2021.

[23] F. Hou, W. Lei, S. Li, and J. Xi, "Deep learning-based subsurface target detection from GPR scans," *IEEE Sensors J.*, vol. 21, no. 6, pp. 8161–8171, Mar. 2021.

[24] Z. Liu, X. Gu, J. Chen, D. Wang, Y. Chen, and L. Wang, "Automatic recognition of pavement cracks from combined GPR B-scan and C-scan images using multiscale feature fusion deep neural networks," *Automat. Construction*, vol. 146, 2023, Art. no. 104698.

[25] H. Chen, P. Tiňo, A. Rodan, and X. Yao, "Learning in the model space for cognitive fault diagnosis," *IEEE Trans. Neural Netw. Learn. Syst.*, vol. 25, no. 1, pp. 124–136, Jan. 2014.

[26] Z. Gong, H. Chen, B. Yuan, and X. Yao, "Multiobjective learning in the model space for time series classification," *IEEE Trans. Cybern.*, vol. 49, no. 3, pp. 918–932, Mar. 2019.

[27] J. Wu, X. Zhou, and Q. Chen, "A characteristic of speaker's audio in the model space based on adaptive frequency scaling," in *Proc. 8th Int. Conf. Big Data Inf. Analytics*, 2022, pp. 99–103.

[28] H. Chen, P. Tiňo, and X. Yao, "Cognitive fault diagnosis in tennessee eastman process using learning in the model space," *Comput. Chem. Eng.*, vol. 67, pp. 33–42, 2014.

[29] H. Chen, F. Tang, P. Tino, A. G. Cohn, and X. Yao, "Model metric co-learning for time series classification," in *Proc. 24th Int. Joint Conf. Artif. Intell.*, 2015, pp. 3387–3394.

[30] G. Olhoeft, "Maximizing the information return from ground penetrating radar," *J. Appl. Geophys.*, vol. 43, no. 2, pp. 175–187, 2000.

[31] A. Strange, V. Chandran, and J. Ralston, "Signal processing to improve target detection using ground penetrating radar," in *Proc. 4th Australas. Workshop Signal Process. Appl.*, 2002, pp. 139–143.

[32] K. He, X. Zhang, S. Ren, and J. Sun, "Deep residual learning for image recognition," in *Proc. IEEE Conf. Comput. Vis. Pattern Recognit.*, 2016, pp. 770–778.

[33] B. Koonce and B. Koonce, "Resnet 50," in *Proc. Convolutional Neural Netw. Swift TensorFlow: Image Recognit. Dataset Categorization*, 2021, pp. 63–72.

[34] S. Liu and W. Deng, "Very deep convolutional neural network based image classification using small training sample size," in *Proc. 3rd IAPR Asian Conf. Pattern Recognit.*, 2015, pp. 730–734.

Nan Deng received the bachelor's and master's degrees in safety engineering from Northeastern University, Shenyang, China, in 2003 and 2006, respectively, and the Ph.D. degree in safety engineering from the Beijing Institute of Technology, Beijing, China, in 2012.

He is currently an Associate Researcher with the Institute of Urban Systems Engineering, Beijing Academy of Science and Technology, Beijing, China. His research interests include method and technology for operation and safety management of urban underground Infrastructures.

Yanxia Wang received the bachelor's degree in information management and information system and master's degree in management science and engineering from the Beijing University of Chemical Technology, Beijing, China, in 2009 and 2012, respectively.

She is currently an Associate Researcher with the Institute of Urban Systems Engineering, Beijing Academy of Science and Technology, Beijing, China. Her research interests include method and technology for operation and safety management of underground pipelines and utility tunnel.

Xuejun Tian received the bachelor's degree in surveying and mapping engineering from the Heilongjiang Institute of Technology, Harbin, China, in 2012.

He is currently a Senior Engineer with the Geophysical Exploration Academy of China Metallurgical Bureau, Baoding, China. His research interests include underground space information nondestructive testing, and data processing and analysis.

Kehui Liu received the bachelor's degree in civil engineering from Central South University, Changsha, China, in 2000, the master's degree in management science and engineering from the Beijing University of Chemical Technology, Beijing, China, in 2007, and the Ph.D. degree in management science and engineering from the Beijing Institute of Technology, Beijing, China, in 2017.

She is currently a Researcher with the Institute of Urban Systems Engineering, Beijing Academy of Science and Technology, Beijing, China. Her research interests include information collection, data analysis, operation management, and safety management methods for urban underground Infrastructures.

Jian Cheng received the B.Sc. degree in automation, the M.Sc. degree in control theory and control engineering, and the Ph.D. degree in communication and information system from the China University of Mining and Technology, Xuzhou, China, in 1997, 2003, and 2008, respectively.

He is currently a Professor and the Chief Scientist with Central Research Institute, China Coal Research Institute, Beijing, China. His research interests include machine learning and pattern recognition.